

A targeted search for strongly lensed supernovae and expectations for targeted searches in the Rubin era

PETER CRAIG,¹ KYLE O'CONNOR,² SUKANYA CHAKRABARTI,^{1,3} STEVEN A. RODNEY,² JUSTIN R. PIEREL,⁴
CURTIS MCCULLY,⁵ AND ISMAEL PEREZ-FOURNON^{6,7}

¹*Rochester Institute of Technology, Rochester, NY 14623*

²*University of South Carolina, 712 Main St., Columbia, SC 29208, USA*

³*Institute for Advanced Study, Princeton, NJ 08540*

⁴*Space Telescope Science Institute, Baltimore, MD 21218*

⁵*Las Cumbres Observatory, 6740 Cortona Dr Ste 102, Goleta, CA 93117-5575, USA*

⁶*Instituto de Astrofísica de Canarias, C/Vía Láctea, s/n, E-38205 San Cristóbal de La Laguna, Tenerife, Spain*

⁷*Universidad de La Laguna, Dpto. Astrofísica, E-38206 San Cristóbal de La Laguna, Tenerife, Spain*

(Received November 3, 2021; Revised November 3, 2021; Accepted November 3, 2021)

ABSTRACT

Gravitationally lensed supernovae (glSNe) are of interest for time delay cosmology and SN physics. However, glSNe detections are rare, owing to the intrinsic rarity of SN explosions, the necessity of alignment with a foreground lens, and the relatively short window of detectability. We present the Las Cumbres Observatory Lensed Supernova Search, LCOLSS, a targeted survey designed for detecting glSNe in known strong-lensing systems. Using cadenced r' -band imaging, LCOLSS targeted 112 galaxy-galaxy lensing systems with high expected SN rates, based on estimated star formation rates. No plausible glSN was detected by LCOLSS over two years of observing. The analysis performed here measures a detection efficiency for these observations and runs a Monte Carlo simulation using the predicted supernova rates to determine the expected number of glSN detections. The results of the simulation suggest an expected number of detections and 68% Poisson confidence intervals, $N_{SN} = 0.20, [0, 2.1]$, $N_{Ia} = 0.08, [0, 2.0]$, $N_{CC} = 0.12, [0, 2.0]$, for all SN, Type Ia, and core-collapse (CC) SNe respectively. These results are broadly consistent with the absence of a detection in our survey. Analysis of the survey strategy can provide insights for future efforts to develop targeted glSN discovery programs. We thereby forecast expected detection rates for the Rubin observatory for such a targeted survey, finding that a single visit depth of 24.7 mag with the Rubin observatory will detect 0.63 ± 0.38 SNe per year, with 0.47 ± 0.28 core collapse SNe per year and 0.16 ± 0.10 Type Ia SNe per year.

Keywords: transients: supernovae — gravitational lensing: strong — (cosmology:) cosmological parameters — surveys

1. INTRODUCTION

Supernovae (SNe) are violent explosions of dying stars. One class of SNe, known as Type Ia SNe, are useful tools in cosmology because they are bright standard candles. The luminosity of Type Ia SNe can be determined accurately from their lightcurves Phillips (1993). Measurements of distance moduli against redshifts in the Hubble flow region provides a measure of

the Hubble Constant, H_0 , the current expansion rate of the Universe. Extending this diagram of Type Ia SNe distances to high redshift gave the first evidence for accelerated expansion in the Universe Riess et al. (1998); Perlmutter et al. (1999). Better measurements of this expansion rate are critically needed due to statistically significant disagreement between measurements of the Hubble constant from analysis of the cosmic microwave background (CMB) (Planck Collaboration et al. 2020) and from analysis of Type Ia SNe at low redshift (Zhang et al. 2017; Wong et al. 2020).

SNe of all types can provide cosmological constraints when multiply-imaged by strong gravitational lensing

(Refsdal 1964). When aligned with a massive foreground object, the light from the SN will be deflected as it passes through the gravitational potential. In the *strong lensing* regime the background object may be observed as multiple distinct images on the sky, each arriving at the observer with relative time delays that can range from hours to years. Measurement of the relative time delays, combined with a model of the lensing potential, allows for a measurement of H_0 and other cosmological parameters. Lensed quasars have been used in this way for many years (Suyu et al. 2018). SN time-delays are attractive additions to the cosmologist’s toolkit, owing primarily to the predictability of their light curves. They also have shorter observing timescales and can provide Type Ia SN luminosity distance measurements to break the mass-sheet degeneracy (Oguri & Kawano 2003).

To date, only three strongly-lensed SNe have been observed with resolved multiple images and measurable time delays (Kelly et al. 2016; Goobar et al. 2017; Rodney et al. 2021). However, this sample is expected to grow dramatically with discoveries from new transient surveys using the Vera Rubin Observatory and the Roman Space Telescope (Goldstein & Nugent 2016; Wojtak et al. 2019; Pierel et al. 2021). These high-cadence, wide-field surveys may detect hundreds of gLSNe over the next decade, though the majority will have relatively short time delays and small angular separations (Pierel et al. 2021; Huber et al. 2019).

An alternate approach for hunting gLSNe is to monitor a sample of known strong-lensing systems, which is the strategy that we adopted with LCOLSS. With the release of the SLACS sample (Bolton et al. 2008), the SWELLS sample of lensed spiral galaxies (Treu et al. 2011; Brewer et al. 2012), the SLACS for the Masses Survey (S4TM) (Shu et al. 2017), and the BELLS sample (Brownstein et al. 2012), we have a sufficiently large number of known strong-lensing systems at low redshift ($z < 1$) that can plausibly yield a detection over \sim year timescales. Most of these galaxies have been presented in Shu et al. (2018) (hereafter S18), which examined a sample of 108 galaxy-galaxy strong lensing systems (i.e., the sources in SLACS, S4TM and BELLS, 98 of which are included in our sample) in which the lens is an early type galaxy and the background galaxy has strong star formation. The high SFRs of the lensed galaxies should result in a higher rate of SN explosions (including Type Ia), and the lensing galaxies with large Einstein radii would result in longer observable time delays with a relatively simple lensing mass profile (Li et al. 2011; Oguri 2019). We present the (null) results of our pilot gLSNe search program here. The goal of LCOLSS was to detect a strongly lensed SN at low redshift (our sample has

an average source redshift of 0.66), which would provide a measurement of the Hubble constant, H_0 from time-delays. The time delay is primarily sensitive to H_0 in contrast to supernovae that yield relative luminosity distances (Suyu et al. 2017).

Our inclusion of the SWELLS sample of lensed spirals was motivated by the goal of determining two *independent* constraints on the dark matter distribution from strong lensing and from analysis of HI maps (Chakrabarti & Blitz 2009, 2011; Chakrabarti et al. 2011; Chakrabarti 2013), which is only possible at low-redshift where HI maps can be obtained. To date, there is only one detection of HI in emission in a known strong spiral lens (Lipnick et al. 2018), though we may expect detections and HI maps of strong spiral lenses from next-generation HI surveys with the Square Kilometer Array (SKA) (Catinella & Cortese 2015; Giovanelli & Haynes 2015). The highest redshift HI map thus far of a non-lensed starburst galaxy was obtained by Fernández et al. (2016) at $z = 0.376$.

The layout of this paper is as follows: In Section 2 the setup and parameters of the LCOLSS survey are described. This includes the strong lens galaxy-galaxy systems being studied, the LCO network, exposure imaging strategy, and difference imaging software. In Section 3, we describe our adopted methods of calculating gLSN yields. These calculations are done two different ways, based upon estimating the detection efficiency of LCOLSS. To check this we compare our photometry to that reported in SDSS. We discuss our results in Section 4; in particular we discuss our expected detection rate for our survey and we estimate Rubin’s detection rate were it to observe the LCOLSS sample. We also very roughly estimate ZTF’s detection rate for a similar sample of galaxies. Finally, we summarize our results and discuss in Section 5.

2. LCO SURVEY

2.1. Lensing Systems

Our sample includes 112 strong-lensing systems. Some useful details for these systems are provided in Appendix A, including an important correction to the SN rates. In S18 the SFR estimates were derived from emission line flux density measurements, but an error in the calculation resulted in an *overestimation* of the inferred SFRs, proportional to $(1+z)^2$ (Shu et al. 2021). We have corrected for this error and propagated it through to also correct the inferred Type Ia and Core Collapse (CC) SN rates, including all the sub-types of CC SNe. The net result is a change of $-5.53 \text{ SNe yr}^{-1}$ in the expected total SN explosion rate, summed over the 98 S18 sources in our sample. Appendix A also includes information

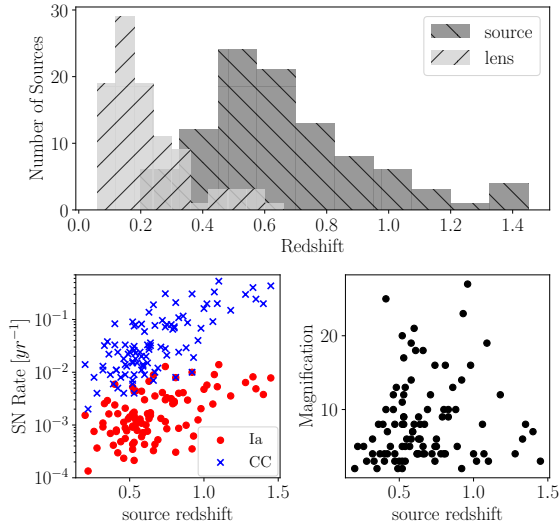


Figure 1. The top panel shows the redshift distribution for our 98 targets, with lensing galaxies in light grey and lensed background galaxies in dark grey. The bottom left panel shows the predicted (observer frame) SN rates for each of the lensed source galaxies, plotted against redshift. Each of the lensed source galaxies appears twice: in red for the Type Ia SN rate and in blue for the CC SN rate. The bottom right panel shows lensing magnifications of each of the systems, plotted against source redshift. See Appendix Table A1 for these values, and (Shu et al. 2018) for details of the redshift measurements, SN rate estimates, and lensing magnifications. Note that the supernova rates here have been corrected for the error in S18 as discussed in section 2.1.

about the number of visits to each source, along with the average seeing and airmass for our observations of each source.

The SN rates are determined from the the star formation rates of the background source galaxies. The star formation rates are measured from observed SDSS and BOSS spectra, using integrated fluxes from [OII] 3727Å emission doublet, $F_{OII}^{\text{intrinsic}} = F_{OII}/\mu/f_{\text{fiber}}$. Determining intrinsic flux in the source galaxy is a multi-step process. The measured flux in the source galaxy, F_{OII} , is extracted from the spectrum centered on the lensing galaxy, with the lensing galaxy spectra subtracted, and a double-gaussian plus line is fit to the [OII] doublet of the remaining source galaxy. The fraction of the source galaxy captured in the spectrograph, f_{fiber} , is then determined using a convolution of the lensed HST image with the PSF from the ground based spectrograph. Finally this value is de-magnified to give the intrinsic flux. The intrinsic flux with [OII] then is calibrated to a SFR, using a subsample for which H α has been detected, as the H α luminosity scales directly with ionizing flux. The

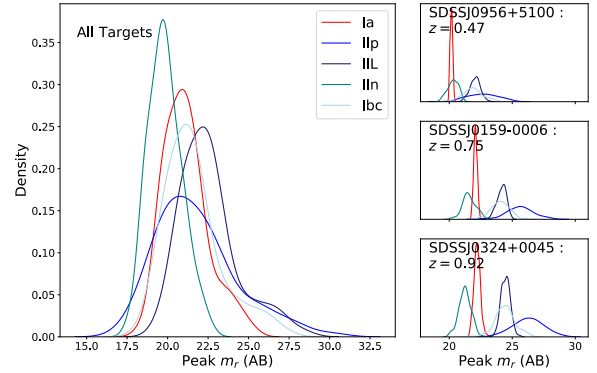


Figure 2. The distributions of peak r-band magnitudes for each SN sub-type, including the lensing magnifications and dust effects. On the left is the distribution corresponding to all of our targets that were included in S18. On the right are a few examples for individual targets at different source redshifts.

uncertainties on the rates based on the flux measurement are large due to the lensing galaxy subtraction, de-magnification, and fiber loss. There are also sources for biases; perhaps the largest being in the inability to perform a system by system H α calibration for the star formation rates; i.e. even before the final models to convert the star formation into SN rates. Another potential source of bias is on the relative core collapse rates which were based on local measurements and assumed to have no redshift evolution, which remains an open question in general Strolger et al. (2020). Although the uncertainties on the supernova rates are large, they are accounted for in the simulation, and very likely provide the best estimate for the expected detection rate.

For more details on the redshift measurements, SN rate estimates, and lensing magnifications, shown in Figure 1, see Shu et al. (2018) and Shu et al. (2017). The resulting distributions of the peak brightness, in the r' filter, for the various SN types are shown in Figure 2.

2.2. Observations

The Las Cumbres Observatory is a robotic telescope network designed for time-domain astronomy (Brown et al. 2013). For the LCOLSS we used the 1-meter LCO telescopes and Sinistro cameras, typically collecting three 300s exposures per target through the r' filter. We reached 3σ limiting magnitudes ranging from ~ 21 - 23 AB mags. We generated difference images using the software tools `pyDIA` Albrow (2017) and `Hotpants` Becker (2013). Each difference image was visually inspected for potential transient sources by at least two

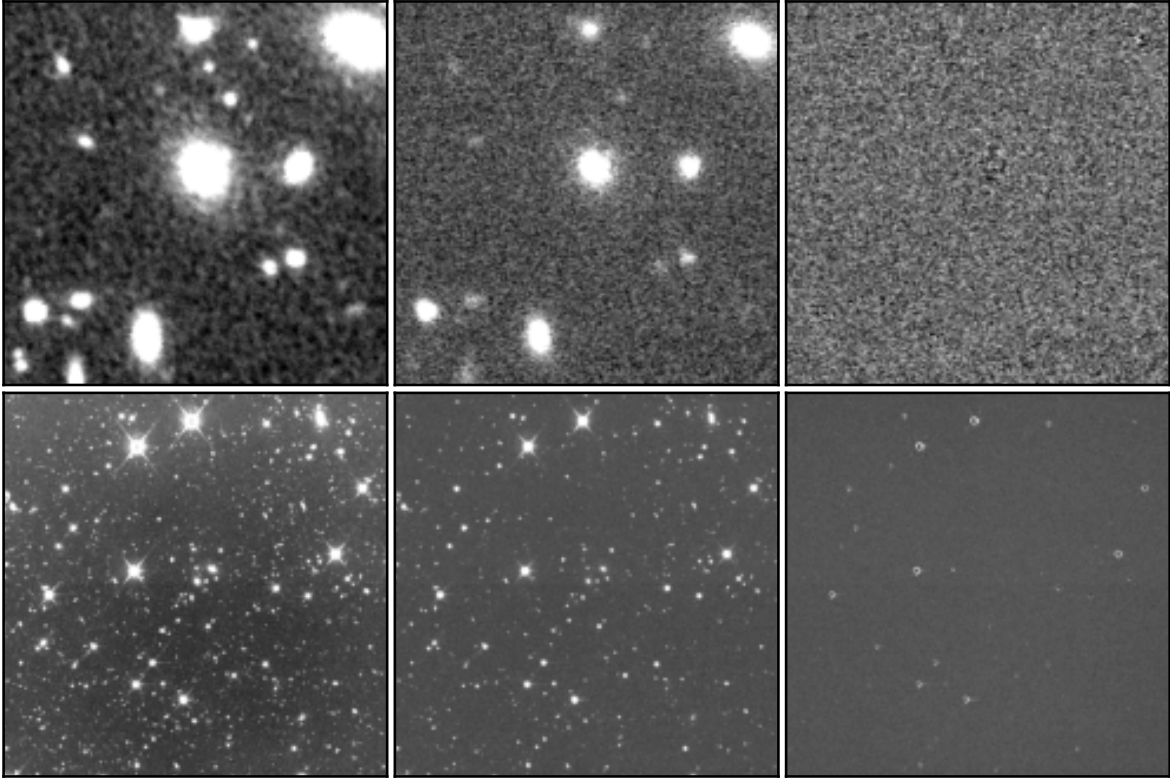


Figure 3. This figure shows an example of a Pydia generated difference image. The left column shows the template, the middle column shows the search image, and the right column shows the difference image. The top row shows a cutout around the target, while the bottom row shows the entire image. The artifacts in the bottom right panel are remnants of bright stars being subtracted from themselves, and are not transient sources.

team members. An example difference image generated by pyDIA can be seen in Figure 3. Our difference imaging search process was validated with detections of numerous solar system bodies with various magnitudes. Our photometric accuracy was confirmed by comparing our photometry with SDSS magnitudes, with results displayed in Figure 4, which shows that the magnitudes from our LCO observations are in good agreement with SDSS magnitudes. In this case the distribution of magnitude differences has a mean of 0.0057 with a standard deviation of 0.052. We derived zero points for each image by matching detected stars to SDSS, limited to the magnitude interval $r' = [16, 20]$ to ensure high signal to noise and no saturation effects.

The depths predicted by the Las Cumbres Observatory Exposure Time Calculator (<https://exposure-time-calculator.lco.global/>) for our observations, with various lunar phases, are shown in Figure 5. Our exposure times varied based on our rate of time usage (relative to the time award in a given semester),

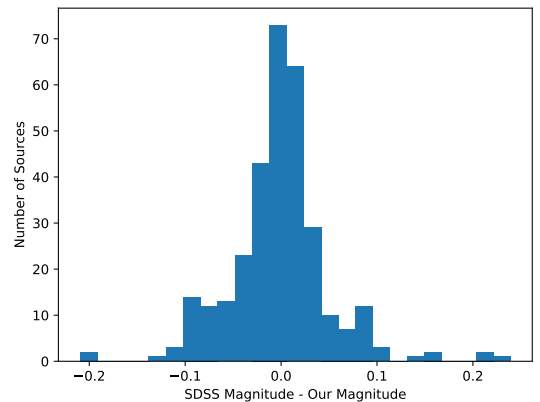


Figure 4. This figure displays some sample zero-point calibration data for a single data frame. This histogram shows the distribution of the differences between our measured magnitudes and those displayed in the SDSS catalog. This indicates that the image zero-point has been correctly determined and that our measurements for the photometry are reasonably accurate.

typically either increasing the exposure time to 600 seconds per frame or reducing the number of frames by one. We calibrated our image processing pipeline by planting fake sources into the images and measuring the recovery efficiency as a function of magnitude. These results demonstrated good agreement with the LCO exposure time calculator (ETC) and we therefore use the ETC estimates for results below. Using our direct measurements of the detection efficiency would result in no significant change in our conclusions.

3. METHODS

We calculate the expected LCOLSS gravitationally lensed SN yields by determining the detection efficiencies of the LCO images, and applying Monte Carlo simulations for the lensed host galaxy supernovae.

3.1. Measuring the SN Detection Efficiency

To determine the expected number of SN detections in our survey, we need to know the detection efficiency, the magnitude dependent ratio between the number detected sources and the total number of sources. We do this following the methods of (Strolger et al. 2015). A commonly used efficiency curve assumes that any supernova brighter than a given magnitude is detected. For instance, in our survey such an assumption would be that for our deep images any supernova with an apparent magnitude of 23 or brighter is detected, while in reality a 23rd magnitude source may be difficult to detect.

We apply here a more robust method by planting synthetic point sources into the difference images and subsequently recovering them in the images (we discuss the details of our recovery procedure later in §3.2.1). Following Strolger et al. (2015), the fractional detection efficiency is then fit as an efficiency parametric model with an exponential functional form. The model parameters, m_{50} and α , characterize the magnitude at which an object has a fifty percent chance of being detected, and the steepness of the efficiency fall off, respectively. In other words, we write the fractional detection efficiency, ϵ , as:

$$\epsilon = (1 + e^{\alpha(m-m_{50})})^{-1} \quad (1)$$

where ϵ is the efficiency and m is the apparent magnitude of a source. We chose to be more rigorous with the efficiency method here since the expected yield is so low, and LCO has not been used for any targeted gLSN survey like this before. The zero point and efficiency parameters are fit using a large group ($\gtrsim 700$) of data images. These results are used (in a nearest neighbor interpolation) to measure the detection efficiency for all surveyed images ($\gtrsim 6000$) in the four LCOLSS semesters over which we carried out our observations.

3.2. Zero Point

The first step in determining a detection efficiency is to measure the zero point, ZP, for each image such that fake sources can be realistically planted at different magnitudes. Stars in each LCO image field are matched to SDSS data which have the stellar magnitudes in the identical r' filter. Fluxes for the stars on the LCO images are then measured with both an aperture-photometry and PSF-photometry method. The zero points of the data images are determined as a least squares fit to $m_{sdss} = -2.5 \log_{10} f_{lco}$; where the calibration is restricted to those stars inside the interval $r' = [16, 20]$. This ensures that the calibration stars have a good signal to noise and no saturation.

A gaussian based model, *IntegratedGaussianPRF*, is used for the PSF, available in the *photutils* software. The spread for the model is taken from the full width at half maximum value, `L1FWHM`¹, determined in the LCO pipeline which is available in each image's header (McCully et al. 2018). The background around each known star is determined and subtracted using a localized sigma-clipped standard deviation on image pixels. The flux is then fit for using the amplitude of the model with fixed positions on the background subtracted sources. The aperture method for the flux uses a circle with radius, $r = 2\text{L1FWHM}$, again with a local background subtraction, taken from the sigma-clipped standard deviation on pixels in an annulus extending over $r_{ann} = [r + 5, r + 10]$.

An example of our zero-point calibration results can be seen in Figure 4. This figure displays the difference between the magnitudes from our data and the magnitudes from the SDSS catalog for one data frame. These results indicate that our photometry generally provides good agreement with SDSS magnitudes.

The accuracy that can be expected in predicting a zero point is determined using a nearest neighbor interpolation on the data, over image header parameters, `EXPTIME`, `MOONFRAC`, `MOONALT`, `MOONDIST`, and `AIRMASS`. The difference between the measured zero point and this interpolation method gives a distribution of errors, $\Delta ZP = ZP - ZP_{interp}$, which indicates that a zero point can be determined using the parameters available in an image header alone with an accuracy,

¹ `L1FWHM` is defined by the LCO pipeline as the frame FWHM calculated from the SExtractor detections with very small objects and those with `FLAGS != 0` weeded out. The individual FWHM values are calculated slightly differently than the SExtractor FWHM values, using $\text{FWHM} = 2 * \sqrt{\ln(2)(a^2 + b^2)}$, where a and b are the source extractor parameters for the maximum and minimum spatial RMS. `L1FWHM` is then a clipped and filtered average over all suitable sources in the frame.

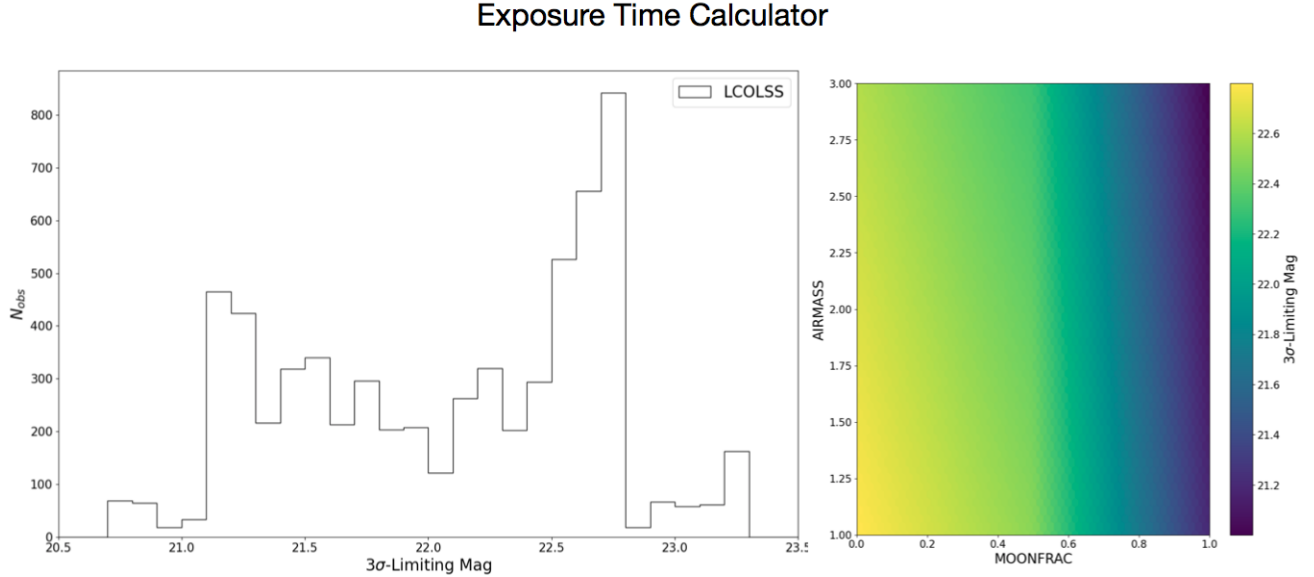


Figure 5. Limiting magnitudes predicted by the Las Cumbres Exposure Time Calculator, ETC <https://exposure-time-calculator.lco.global>. The figure on the left shows the distribution of 3σ limiting magnitudes for the observations in our survey. On the right the colorbar shows the full range of predicted 3σ limiting magnitudes. The predictions are made using an interpolation over the lunar phase and airmass.

$< \Delta ZP > = 0.17$ mag. This provides a computationally inexpensive method to estimate the ZP for a large number of images.

3.2.1. Planting and Recovering Synthetic SNe

After the zero point calibration, the PSF is scaled to different magnitudes and added to the difference image as fake SNe. These images with the synthetic SNe are then used in a threshold based source detection algorithm. The efficiencies are defined as the fraction of synthetic SNe recovered.

These efficiency measurements take advantage of various `photutils` functions. The PSF used, as mentioned earlier, is the *IntegratedGaussianPRF*, which requires only the spread taken from the image headers. The planting of the PSF in the image at various positions and fluxes is done using *subtract_psf*. The fluxes of the synthetic SNe that we have planted are determined using the zero point, at magnitudes covering $r = [20.5, 23.5]$. The synthetic SNe are planted in a twenty five position lattice configuration around the lensing galaxy. These sources are separated by 25 pixels, which covers a total area of 0.42 square arcminutes, with a scale of $0.389''$ per pixel. At the redshift of our sample, this covers a physical distance of tens to hundreds of kpc, so would represent any possible SNe within the galaxy, including as well SNe that form in the outskirts of galaxies (Chakrabarti et al. 2018). The lattice is centered on the target, and does not vary based on source properties. In

determining the recovery for the fake planted sources, we have used *DAOSStarFinder* with a 3σ -threshold, where σ is the difference image noise taken as the sigma-clipped standard deviation. This method looks for sources that have at least 5 adjacent pixels above the given threshold. A linear least squares method is applied to the recovered fractions at the given magnitudes to determine the parameters m_{50} and α in the efficiency function, Equation 1.

An example showing the planting of SNe into a difference image and the measured efficiency are shown in Figure 6. This is for one data frame that has a measured m_{50} of 22.01, and shows the measured efficiency as a function of magnitude. The case with a source magnitude of 22 is shown in the bottom left, where close to half of the synthetic sources are detected. The source detection software was set to agree with those objects which would have likely received close attention; which can be seen in Figure 6.

3.3. Efficiency Results

The resulting efficiency curves, corresponding to fractions of recovered sources at different magnitudes, are shown for the fitted image data in Figure 7. The depth characterized by m_{50} is in general agreement with the predictions made by the exposure time calculator (e.g., Figure 5). These observations typically detect transients around $r \approx 21$, but the depth rarely reaches much past $r \approx 23$. There seems to be a small shift to lower limiting

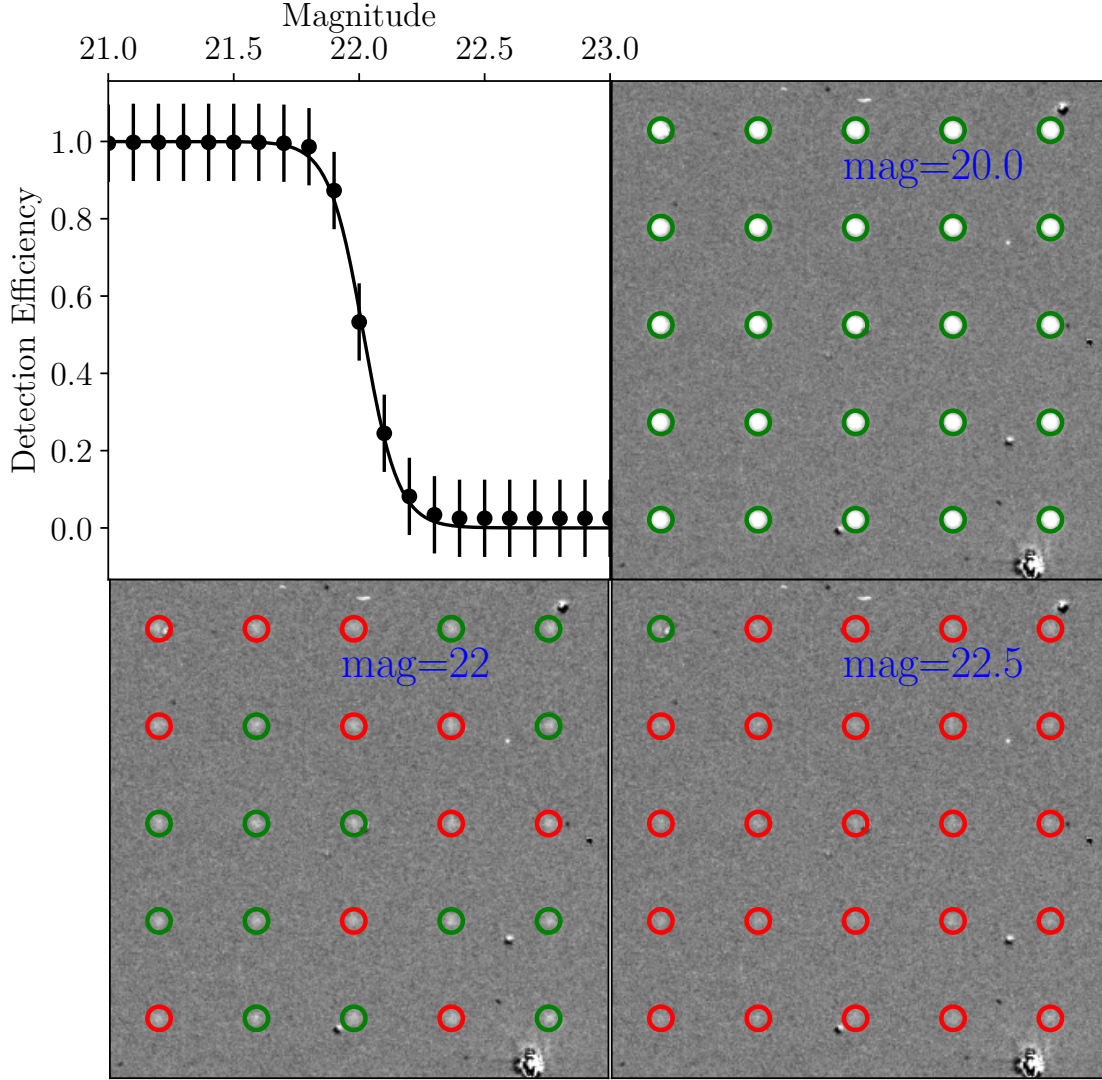


Figure 6. An example of the efficiency measurement is shown above. The top left figure shows both the measured detection efficiencies and our best fitting curve from Equation 1. The top right image has plants with magnitudes which would provide a near certain detection. On the bottom left is an image with plants at magnitude near the fifty percent efficiency value. The bottom right has plants with magnitudes faint enough that detection would be unlikely. Green and red circles mark the locations of the plants and signify detected and missed objects respectively.

magnitude; it is occasionally difficult to detect sources around $r \approx 20.5$. The steepness of the efficiency drop-off, α , indicates that a point source limiting magnitude in a given observation drops from a likely to unlikely detection on the order of ~ 0.5 mag.

The measured m_{50} and α detection efficiency values are used along with image header parameters EXPTIME, MOONFRAC, MOONALT, MOONDIST, AIRMASS,

L1MEAN, L1FWHM in another nearest neighbor interpolation to predict the efficiencies. The distribution of errors from these, $\Delta m_{50} = m_{50} - m_{50,interp}$ and $\Delta \alpha = \alpha - \alpha_{interp}$, provide a confidence in our ability to assign efficiencies to the full set of surveyed data in the two years of observations.

3.4. SN Monte Carlo Simulation

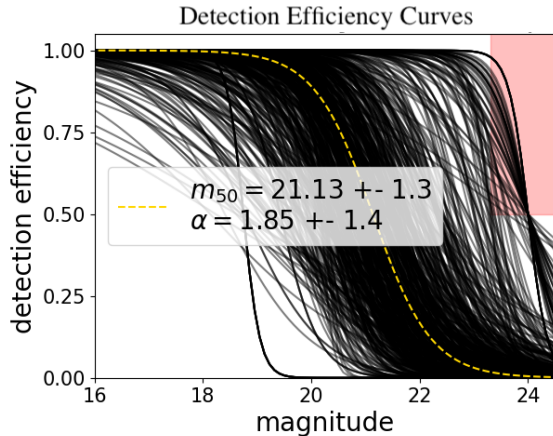


Figure 7. The curves corresponding to the fitted m_{50} and α parameters for Equation 1 on the 572 measured data frames. The dashed gold curve shows the median m_{50} and α curve. The red region highlights those curves which have not been used to assign efficiencies (our observations are unlikely to have detections at those depths), and a conservative value is assigned instead. The median values across this sample are $m_{50} = 21.13 \pm 1.3$ and $\alpha = 1.85 \pm 1.4$.

The population of lensed SNe that could be discovered by LCOLSS was determined by using a Monte Carlo method to generate supernova lightcurves in each target host galaxy. In this calculation, we sample over SN rates, SN spectral-temporal models, the SN intrinsic luminosity, and lensing galaxy magnification. We also include the effects of dust extinction, which is estimated based on the position of the source on the sky. The distributions for these parameters will be defined in this section.

Lightcurves were generated for all the synthetic SNe with each target redshift and magnification using SNCosmo software Barbary (2014); a package with an available library of spectral-temporal models for various SNe types, and which takes into account K correction (conversion to rest frame) and the distance modulus. The SN templates, and normally distributed luminosity functions were selected following Goldstein et al. (2019). The only difference in choice being for the Ia template, where salt2-extended Guy et al. (2007) Pierel et al. (2018), was used, see Table 1.

Dust extinction, was included using the model of Cardelli et al. (1989) (as another built-in feature of SNCosmo) in the lightcurves for both the Milky Way and the host galaxy. In the Milky Way, $E(B - V)$ was assigned using the target coordinates in the map from Schlegel et al. (1998), and $R(V) = 3.1$ following a typical value determined for the diffuse interstellar medium in Cardelli et al. (1989). With the host galaxies, the dust extinction slope, $R(V) = 3.1$, was used again. A

conservative value $A_V = 0.1$ was used as each host’s total extinction. This gives us a total $A_{r'}$ ranging from 0.15 to 0.59, depending on the MW extinction.

Stretch and color parameters, $x1, c$ are required to specify the salt2-extended Ia lightcurves. They characterize the intrinsic Ia drop off in magnitude and $E(B - V)$ at peak. They were allowed to vary, sampled from the asymmetric-Gaussian distributions determined in Scolnic & Kessler (2016). The distribution for $x1$ has a mean of 0.973, with $\sigma_- = 1.472$ and $\sigma_+ = 0.222$. The c distribution has $\mu = -0.054$, $\sigma_- = 0.043$, and $\sigma_+ = 0.101$.

The total number of core collapse SNe, N_{CC} , were divided into sub-types following Eldridge et al. (2013); note that this assumes similar cosmological CC relative rates as those from local measurements, i.e., this assumes no evolution with redshift, which is an open question in general Strolger et al. (2020). The only changes here are the grouping of IIb and IIpec with the III. See Table 2 for these rates and sub-type descriptions.

The key differences between the analysis for expected detections done here and that carried out in Shu et al. (2018) are the updated rates, and true survey data for cadencing and depth. One other difference between the analysis here and that done in Shu et al. (2018) is in the lensing magnifications applied to the SNe; Shu et al. (2018) used a common value of $\mu = 5$ for every one of their systems. As mentioned in their analysis this is a simple² and conservative value with previous discoveries ranging from $\mu = [3, 10]$. In the analysis done here however, the target-specific total lensing values determined in Shu et al. (2017) are used instead. The range covered, $\mu = [2, 105]$, is consistent with both their fiducial value as well as in agreement with previously discovered gISNe.

Our predicted yield is then determined by using the ETC-predicted limiting magnitudes and our internally-derived efficiency curves to count the fraction of SN explosions that would be detected by the LCOLSS. This fraction then provides our total expected SN yield. Our predicted yield over the full survey for the sources in our sample can be seen in Figure 8. This figure also displays the differences between our derived detection efficiency and that determined by the ETC predictions.

4. RESULTS

The intrinsic supernovae data, i.e., the luminosity functions, SN rates, and relative core collapse rates, all have associated uncertainties. These uncertainties are

² Source-plane position being key in the true magnification of a point source object

Table 1. Details of the luminosity functions and templates used for the supernova population model. Originally given in Vega magnitudes in Goldstein et al. (2019) these have been converted to the AB system following the B band shift, $m_{AB} - m_{Vega} = 0.09$, determined in Blanton & Roweis (2007). This table shows the mean and standard deviation for the magnitude distribution for each SN type, as well as references for additional information.

SN Type	μ_{MB}	σ_{MB}	Template	Template Reference	Luminosity Reference
Ia	-19.32	0.10	Salt 2	Guy et al. (2007)	Sullivan et al. (2006)
IIP	-16.99	1.12	SN 2005lc	Sako et al. (2011)	Li et al. (2011)
IIIL	-17.55	0.38	Nugent-IIIL	Gilliland et al. (1999)	Li et al. (2011)
IIIn	-19.14	0.50	Nugent-IIIn	Gilliland et al. (1999)	Li et al. (2011)
Ibc	-17.60	0.74	Nugent-Ibc	Levan et al. (2005)	Li et al. (2011)

Table 2. Relative rates of core collapse SN sub-types from Eldridge et al. (2013). The IIb and Ipec fractions are grouped with IIL template in our analysis.

CC Type	Rel. Rate (%)	Descr.
IIP	55.5	“plateau” of lc, H-shell interactions RSG progenitor
IIIL	3.0 → 26.1	“linear” decay of lc
IIIn	2.4	“narrow” H-lines, interactions with circumstellar material
IIb → IIIL	12.1 → 0.0	H-lines only in early weeks, transitional to Ibc
Ipec → IIIL	1.0 → 0.0	“peculiar” 1987a like, BSG progenitor
Ib	9.0	No H lines, WR progenitor
Ic	17.0	No H or He lines, WR progenitor

Table 3. Total SN detections expected over our 2 year survey with LCO in rp (and yearly); Along with associated probabilities for at least one detection. The numbers assuming various limiting magnitude depths as constants for each observation included as well.

Method	Detections: Total (Yearly) $\overline{SN}, \overline{Ia}, \overline{CC}$	p(SN Detections ≥ 1): Total (Yearly)
Exposure Time Calculator	0.198,0.080,0.117 (0.092,0.037,0.054)	0.179 (0.088)
Efficiency Curve	0.192,0.062,0.13 (0.089,0.029,0.060)	0.174 (0.085)
20-limiting	0.009,0.005,0.004 (0.004,0.002,0.002)	0.01 (0.004)
21-limiting	0.049,0.026,0.023 (0.023,0.012,0.011)	0.048 (0.023)
22-limiting	0.141,0.065,0.076 (0.065,0.030,0.035)	0.131 (0.063)
23-limiting	0.357,0.142,0.215 (0.165,0.066,0.010)	0.300 (0.152)
24-limiting	0.631,0.173,0.458 (0.292,0.080,0.212)	0.468 (0.253)
25-limiting	0.987,0.259,0.728 (0.457,0.120,0.337)	0.627 (0.367)

accounted for in the Monte Carlo simulation we carry out to generate SN lightcurves. The largest uncertainties are for the supernova rates, with a median uncertainty of $\frac{e_{RSN}}{R_{SN}} = 0.60$. The reasons for the large uncertainty are as described in section 2.1.

The redshifts and magnifications of the target data from S18 have smaller uncertainties. The redshifts are all measured spectroscopically, for both the lensing and host galaxies. The average lensing magnifications, μ , are the ratio of total flux mapped onto the image plane to the flux in the source plane. These were determined in Shu et al. (2017) using singular isothermal ellipsoid modeling with the HST F814W images of the

lensed galaxies. The magnifications determined using the modeling done in Shu et al. (2017), were compared to the values from previous models done for the 25 BELLS strong lens systems in Brownstein et al. (2011), $\mu_{ratio} = \mu_{shu2018}/\mu_{brownstein2012}$. The average ratio, $\bar{\mu} = 0.94$, showed good agreement between the independent modeling. The standard deviation of the ratios, $\sigma\mu_{ratio} = 0.16$ is used as the fractional uncertainty for all of the lens modeling.

4.1. Expected SN yields: for LCOLSS & Rubin observations of the LCOLSS galaxies

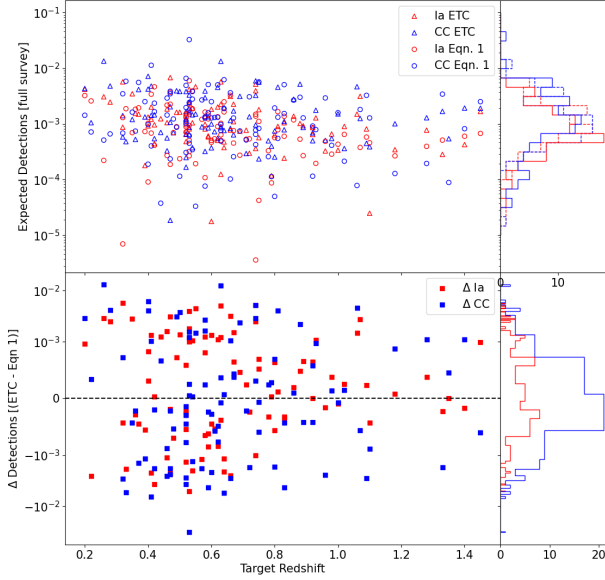


Figure 8. On top, the expected Poisson SN detection numbers in the target galaxies as a function of the redshift. On bottom the difference between the target yields predicted by the Exposure Time Calculator and Equation 1 methods for counting up detected SNe.

For the LCOLSS sample, we find an expected yield and 68% Poisson confidence intervals, $N_{SN} = 0.20, [0, 2.1]$, $N_{Ia} = 0.08, [0, 2.0]$, $N_{CC} = 0.12, [0, 2.0]$ of total SNe, Type Ia, and core-collapse SNe respectively. Our analysis indicates that the null result of the LCOLSS search is not surprising. After correcting the predicted SFRs in the target lensed galaxies, and accounting for the depth achievable with 1-meter class telescopes, we find that the probability of detecting ≥ 1 lensed SN per year with this survey design is < 0.20 . The key improvement for a future targeted SN survey to be successful would be to reach fainter magnitudes with each observation. For example, the 8.4-meter Rubin Observatory will reach an r-band 5σ depth of 24.7 AB mag. Observing a similar sample of ~ 100 strong-lensing systems, Rubin Observatory will have a $> 50\%$ chance of detecting a lensed SN each year. The Rubin Observatory will ultimately observe a larger number of known lensed sources, with 4476 known lensing systems from the masterlens³ catalog within the WFD field. Rubin is expected to recover hundreds to thousands (depending on the image separation) of lensed sources over ten years (Oguri & Marshall 2010; Goldstein & Nugent 2016). If we assume that the number of detections per source per year for our sample is the same for all the known lenses in the masterlens catalog (this assumes

that these lenses have a similar SN rate, redshift and magnification distribution), we would expect 29 detections per year from Rubin for a targeted survey of the ~ 4000 known lenses that will be in the WFD field. Over ten years this predicts 290 detections, which is similar to other estimates (Goldstein & Nugent 2016; Wojtak et al. 2019). This estimate will have a high uncertainty as we are making assumptions about the properties of the sample. A more accurate estimate would require additional information for the source galaxies, such as the star formation rates, redshifts and the magnification of the lensing system. This information is not generally available for these sources, so we estimate that they have similar properties to the LCOLSS sample.

Our analysis can also be used to investigate the trade off between the limiting magnitude and the cadence. We find that the image depth plays a larger role than the cadence on the total yield. The results indicate that changing the cadence from two weeks to four weeks produces the same yield if we increase the image depth by about 0.4 magnitudes. Thus, a deeper survey can provide a better yield even with less frequent observations. However, such a survey is more likely to miss the peak of the SN, and will often have fewer observations by the time follow-up resources get triggered.

Figure 9 shows the expected yearly detection rate in our survey for a variety of limiting magnitudes. This figure also includes the values expected if the Rubin observatory were used instead of LCO for this survey, which reaches deeper limiting magnitudes. In practice, Rubin observatory will not cover much of our source list due to the sky locations of our systems. The sky coverage of Rubin compared to our survey and the masterlens catalog can be seen in Figure 9. In addition to the number of detections per year, this figure includes the Poisson probability of getting a detection in one year of the LCOLSS survey for each magnitude. The uncertainties shown are estimated to be 60% of the detection rate, which is dominated by the uncertainty on the supernova rates. The uncertainty goes up at fainter magnitudes because the detection rate goes up as we become sensitive to fainter supernovae. The uncertainty on our detection efficiency curves is not included in the uncertainties here, as it is expected to be much less than the uncertainty on the supernova rates.

Investigating the expected SN yields for the LCOLSS search could be illuminating for understanding the Zwicky Transient Facility (ZTF) survey. The ZTF has a 47 deg^2 FoV imaging the northern sky every three nights in g and r filters reaching to $m_r \sim 20.5$ at $S/N = 5$. This large scale data is automatically searched to flag transients with roughly 10^6 alerts per night (Graham et al.

³ <http://admin.masterlens.org>

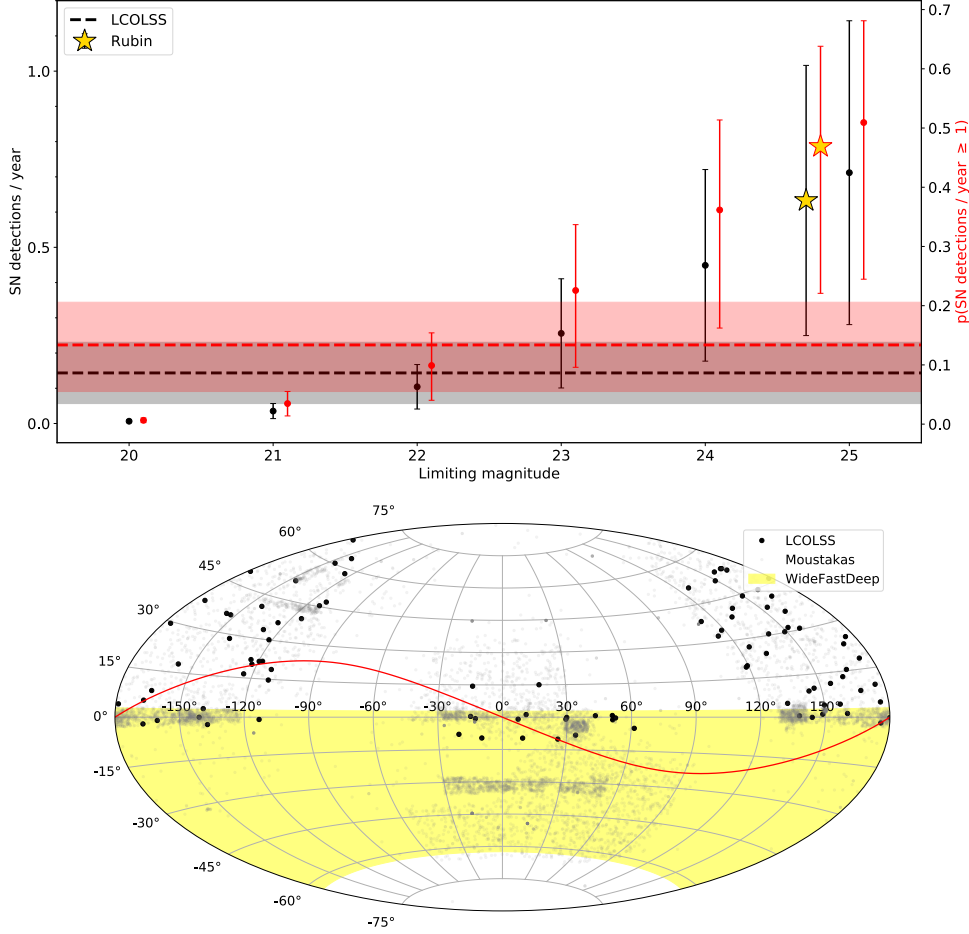


Figure 9. The top figure shows the expected yearly SN detections to come from the LCOLSS survey (in black) and the corresponding Poisson probability of this resulting in at least one SN detection per year (in red). The dashed horizontal lines show the expected value for SN detections/year, (0.14 ± 0.08), using the Exposure Time Calculator. The efficiency curve method (omitted) is in very good agreement. The shaded regions in red and black, correspond to the uncertainties on the expected detections, and the Poisson probabilities at those error bounds. The circular markers show the results assuming constant single visit limiting magnitudes. The gold star provides an estimate corresponding to the values if this survey were carried out using WFD imaging planned with Rubin; single visit (2x15 second) 5 sigma r band depth of 24.7. This estimate assumes that Rubin uses our cadence and set of targets (or a similar set of targets that are within Rubin’s coverage). Below is a map highlighting the region which will be surveyed with Rubin’s Wide Fast Deep survey. The location of the LCOLSS targets are shown in black and a larger catalog of all known lensing systems (Moustakas et al. 2012) in grey. Rubin’s increased depth and exposure, along with known (and to-be discovered) lensing systems, should provide many detections over the 10 year program.

(2019). A possible method is to search for lensed SNe as any SN observed in a quiescent (E/S0) galaxy which exceeds the brightness expected at the galaxies photometric redshift Goldstein et al. (2019), which can select lensed supernovae in systems that are not resolved. This method predicted the ZTF survey would find ~ 8.6 glSNe per year with approximately 1.2 Type Ia, 2.8 Type IIp, 0.3 Type IIL, 0.4 Type Ibc, 3.8 Type IIc, and 0.2 SN 1991T like. If we scale up our expected detection rate for the number of known lenses observed by ZTF, we find a yield of ~ 7 lensed SNe per year. This is over

~ 6700 sources from the masterlens sample covered by ZTF. As with the Rubin estimator, this estimate has a high uncertainty. However, the estimate remains inconsistent with the lack of a ZTF detection assuming a limiting magnitude of 20.5. Unfortunately over several of years of operation, there have been no publicly announced detections, indicating that the actual detection rates are somewhat lower than expected. One may expect that confirmation of possible lensed SN candidates is limited by false positives (one of which may be distinguishing between variable stars and SNe) and spec-

troscopic follow-up of putative lensed SNe candidates. The spectroscopic follow-up has a limiting magnitude of 19 (only complete to 18.5) (Graham et al. 2019), which may well limit possible follow-up observations.

The detection efficiencies were thoroughly investigated through two different methods in the LCOLSS analysis done here; first using the Exposure Time Calculator and again with Equation 1 calibrated on SDSS data. The Exposure Time Calculator counted detections in binary, based on the $S/N=3$ threshold predicted according to image lunar conditions and airmass. In Equation 1 the detections were counted as a fractional chance of recovery, measured on the difference images. The similar yields predicted through both channels suggest that the depths of the images are well accounted for. Perhaps one final project for a future targeted survey would be to test the human searchers with fake plants. The confusion matrix of recovery data (True positive, False positive, True negative, False negative) obtained throughout the program by the searchers, would allow for another sanity check against the efficiency as determined by detection software.

5. SUMMARY AND DISCUSSION

We find an expected number of detections and 68% Poisson confidence intervals, $N_{SN} = 0.20, [0, 2.1]$, $N_{Ia} = 0.08, [0, 2.0]$, $N_{CC} = 0.12, [0, 2.0]$, for all SN, Type Ia, and CC SNe respectively for LCOLSS per year. Thus, our analysis indicates that the null result of the LCOLSS survey is not surprising. We estimate that the detection rate based on our data is relatively low, such that a significantly longer survey time or deeper limiting magnitudes for the survey would be required in order to expect a detection with this configuration. We also estimated the expectation for the SN yield if the cadence were to be lowered to once per month, instead of our standard two-week cadence. Such a strategy would produce the same lensed SN yield if the limiting magnitude were increased by 0.4 magnitudes, indicating that the depth of the survey is the dominant factor in determining the lensed SN yield. For the same survey time (and cadence), detecting fainter SNe would make the largest difference to the SN yields for a targeted survey. The ZTF search strategy is very different to the one outlined here, and there is a larger difference (nearly a factor of ten) between expected SN yields and actual SN yields. For a targeted search such as this one, follow-up of possible SN candidates can be more straightforwardly allocated resources on the basis of the quality of the difference images, given that we know that the source is lensed. This more straightforward correspondence between expected SN yields and actual detections suggests that discover-

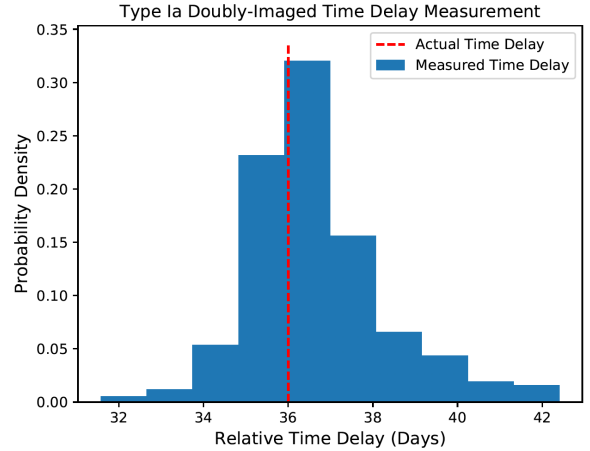


Figure 10. This histogram displays the expected time delay distribution for the lensing systems in our sample. The average time delay anticipated is about 36 days.

ing a lensed SN may be more easily realized in a targeted search.

Although the LCOLSS did not produce any SN detections, our analysis here shows that a targeted survey at fainter limiting magnitudes is likely to yield a detection over one year timescales. This dominant dependence on the limiting magnitude suggests that detections of lensed SNe are more likely achieved on larger telescopes even if the observations are more infrequent (\sim once a month) than our adopted cadence. One can also estimate to what level we would have been able to constrain H_0 , given the time delays for this sample, had we obtained a detection. The average expected time delays for this sample are about 36 days, with a distribution that can be seen in Figure 10. The precision on the time delays with this data alone is about 5% and 7% for Type Ia and core-collapse SNe respectively (and therefore a roughly comparable uncertainty on H_0 assuming the uncertainty on the lens models does not exceed the precision on the time delays) if a detection is guaranteed before the peak. Here, we have followed the formalism in Pierel & Rodney (2019) to calculate time-delays for our sample. The current and future high cadence transient surveys, ZTF and Rubin, discussed in section 1, are/will be greatly increasing SN detection numbers. In addition to these, next generation space telescopes, particularly the Roman Space Telescope, are expected to discover large numbers of SNe at higher redshifts (Pierel et al. 2021).

ACKNOWLEDGMENTS

SC gratefully acknowledges support from the RCSA Time Domain Astrophysics Scialog award, NASA ATP NNX17AK90G, NSF AAG 2009574, and the IBM Einstein Fellowship from the Institute for Advanced Study. SC also gratefully acknowledges time awards LCO2020B-015, LCO2020A-019, LCO2019B-022, LCO2019A-008 on which this work is based. IPF acknowledges support from the Spanish State Research Agency (AEI) under grant numbers ESP2017-86852-C4-2-R and PID2019-105552RB-C43. We thank Yiping Shu, Leonidas Moustakas and Peter Nugent for many helpful discussions.

DATA AVAILABILITY

The data underlying this article will be shared on reasonable request to the corresponding author.

REFERENCES

- Albrow, M. D. 2017, pyDIA.
<http://doi.org/10.5281/zenodo.268049>
- Barbary, K. 2014, sncosmo.
<https://doi.org/10.5281/zenodo.592747>
- Becker, A. 2013, hotpants.
<https://github.com/acbecker/hotpants>
- Blanton, M. R., & Roweis, S. 2007, *The Astronomical Journal*, 133, 734, doi: [10.1086/510127](https://doi.org/10.1086/510127)
- Bolton, A. S., Treu, T., Koopmans, L. V. E., et al. 2008, *ApJ*, 684, 248, doi: [10.1086/589989](https://doi.org/10.1086/589989)
- Brewer, B. J., Dutton, A. A., Treu, T., et al. 2012, *MNRAS*, 422, 3574, doi: [10.1111/j.1365-2966.2012.20870.x](https://doi.org/10.1111/j.1365-2966.2012.20870.x)
- Brown, T. M., Baliber, N., Bianco, F. B., et al. 2013, *PASP*, 125, 1031, doi: [10.1086/673168](https://doi.org/10.1086/673168)
- Brownstein, J. R., Bolton, A. S., Schlegel, D. J., et al. 2011, *The Astrophysical Journal*, 744, 41, doi: [10.1088/0004-637X/744/1/41](https://doi.org/10.1088/0004-637X/744/1/41)
- Brownstein, J. R., Bolton, A. S., Schlegel, D. J., et al. 2012, *ApJ*, 744, 41, doi: [10.1088/0004-637X/744/1/41](https://doi.org/10.1088/0004-637X/744/1/41)
- Cardelli, J. A., Clayton, G. C., & Mathis, J. S. 1989, *The Astrophysical Journal*, 345, 245, doi: [10.1086/167900](https://doi.org/10.1086/167900)
- Catinella, B., & Cortese, L. 2015, *MNRAS*, 446, 3526, doi: [10.1093/mnras/stu2241](https://doi.org/10.1093/mnras/stu2241)
- Chakrabarti, S. 2013, *ApJ*, 771, 98, doi: [10.1088/0004-637X/771/2/98](https://doi.org/10.1088/0004-637X/771/2/98)
- Chakrabarti, S., Bigiel, F., Chang, P., & Blitz, L. 2011, *ApJ*, 743, 35, doi: [10.1088/0004-637X/743/1/35](https://doi.org/10.1088/0004-637X/743/1/35)
- Chakrabarti, S., & Blitz, L. 2009, *MNRAS*, 399, L118, doi: [10.1111/j.1745-3933.2009.00735.x](https://doi.org/10.1111/j.1745-3933.2009.00735.x)
- . 2011, *ApJ*, 731, 40, doi: [10.1088/0004-637X/731/1/40](https://doi.org/10.1088/0004-637X/731/1/40)
- Chakrabarti, S., Dell, B., Graur, O., et al. 2018, *ApJL*, 863, L1, doi: [10.3847/2041-8213/aad0a4](https://doi.org/10.3847/2041-8213/aad0a4)
- Eldridge, J. J., Fraser, M., Smartt, S. J., Maund, J. R., & Crockett, R. M. 2013, *Monthly Notices of the Royal Astronomical Society*, 436, 774, doi: [10.1093/mnras/stt1612](https://doi.org/10.1093/mnras/stt1612)
- Fernández, X., Gim, H. B., van Gorkom, J. H., et al. 2016, *ApJL*, 824, L1, doi: [10.3847/2041-8205/824/1/L1](https://doi.org/10.3847/2041-8205/824/1/L1)
- Gilliland, R. L., Nugent, P. E., & Phillips, M. M. 1999, *The Astrophysical Journal*, 521, 30, doi: [10.1086/307549](https://doi.org/10.1086/307549)
- Giovanelli, R., & Haynes, M. P. 2015, *A&A Rv*, 24, 1, doi: [10.1007/s00159-015-0085-3](https://doi.org/10.1007/s00159-015-0085-3)
- Goldstein, D. A., & Nugent, P. E. 2016, *The Astrophysical Journal*, 834, L5, doi: [10.3847/2041-8213/834/1/L5](https://doi.org/10.3847/2041-8213/834/1/L5)
- Goldstein, D. A., Nugent, P. E., & Goobar, A. 2019, *The Astrophysical Journal Supplement Series*, 243, 6, doi: [10.3847/1538-4365/ab1fe0](https://doi.org/10.3847/1538-4365/ab1fe0)
- Goobar, A., Amanullah, R., Kulkarni, S. R., et al. 2017, *Science*, 356, 291, doi: [10.1126/science.aal2729](https://doi.org/10.1126/science.aal2729)
- Graham, M. J., Kulkarni, S. R., Bellm, E. C., et al. 2019, *Publications of the Astronomical Society of the Pacific*, 131, 078001, doi: [10.1088/1538-3873/ab006c](https://doi.org/10.1088/1538-3873/ab006c)
- Graham, M. J., Kulkarni, S. R., Bellm, E. C., et al. 2019, *PASP*, 131, 078001, doi: [10.1088/1538-3873/ab006c](https://doi.org/10.1088/1538-3873/ab006c)
- Guy, J., Astier, P., Baumont, S., et al. 2007, *Astronomy & Astrophysics*, 466, 11, doi: [10.1051/0004-6361:20066930](https://doi.org/10.1051/0004-6361:20066930)
- Huber, S., Suyu, S. H., Noebauer, U. M., et al. 2019, *A&A*, 631, A161, doi: [10.1051/0004-6361/201935370](https://doi.org/10.1051/0004-6361/201935370)
- Kelly, P. L., Brammer, G., Selsing, J., et al. 2016, *The Astrophysical Journal*, 831, 205, doi: [10.3847/0004-637X/831/2/205](https://doi.org/10.3847/0004-637X/831/2/205)
- Levan, A., Nugent, P., Fruchter, A., et al. 2005, *The Astrophysical Journal*, 624, 880, doi: [10.1086/428657](https://doi.org/10.1086/428657)
- Li, W., Chornock, R., Leaman, J., et al. 2011, *MNRAS*, 412, 1473, doi: [10.1111/j.1365-2966.2011.18162.x](https://doi.org/10.1111/j.1365-2966.2011.18162.x)

- Li, W., Leaman, J., Chornock, R., et al. 2011, *Monthly Notices of the Royal Astronomical Society*, 412, 1441, doi: [10.1111/j.1365-2966.2011.18160.x](https://doi.org/10.1111/j.1365-2966.2011.18160.x)
- Lipnick, A., Chakrabarti, S., Wright, M. C. H., et al. 2018, *MNRAS*, 476, 3097, doi: [10.1093/mnras/sty326](https://doi.org/10.1093/mnras/sty326)
- McCully, C., Volgenau, N. H., Harbeck, D.-R., et al. 2018, *Software and Cyberinfrastructure for Astronomy V*, 22, doi: [10.1117/12.2314340](https://doi.org/10.1117/12.2314340)
- Moustakas, L. A., Brownstein, J., Fadely, R., et al. 2012, in *American Astronomical Society Meeting Abstracts*, Vol. 219, American Astronomical Society Meeting Abstracts #219, 146.01
- Oguri, M. 2019, *Reports on Progress in Physics*, 82, 126901, doi: [10.1088/1361-6633/ab4fc5](https://doi.org/10.1088/1361-6633/ab4fc5)
- Oguri, M., & Kawano, Y. 2003, *MNRAS*, 338, L25, doi: [10.1046/j.1365-8711.2003.06290.x](https://doi.org/10.1046/j.1365-8711.2003.06290.x)
- Oguri, M., & Marshall, P. J. 2010, *MNRAS*, 405, 2579, doi: [10.1111/j.1365-2966.2010.16639.x](https://doi.org/10.1111/j.1365-2966.2010.16639.x)
- Perlmutter, S., Turner, M. S., & White, M. 1999, *Physical Review Letters*, 83, 670, doi: [10.1103/PhysRevLett.83.670](https://doi.org/10.1103/PhysRevLett.83.670)
- Phillips, M. M. 1993, *The Astrophysical Journal Letters*, 413, L105, doi: [10.1086/186970](https://doi.org/10.1086/186970)
- Pierel, J. D. R., & Rodney, S. 2019, *ApJ*, 876, 107, doi: [10.3847/1538-4357/ab164a](https://doi.org/10.3847/1538-4357/ab164a)
- Pierel, J. D. R., Rodney, S., Vernardos, G., et al. 2021, *ApJ*, 908, 190, doi: [10.3847/1538-4357/abd8d3](https://doi.org/10.3847/1538-4357/abd8d3)
- Pierel, J. D. R., Rodney, S., Avelino, A., et al. 2018, *Publications of the Astronomical Society of the Pacific*, 130, 114504, doi: [10.1088/1538-3873/aadb7a](https://doi.org/10.1088/1538-3873/aadb7a)
- Planck Collaboration, Aghanim, N., Akrami, Y., et al. 2020, *A&A*, 641, A6, doi: [10.1051/0004-6361/201833910](https://doi.org/10.1051/0004-6361/201833910)
- Refsdal, S. 1964, . . , 128, 12
- Riess, A. G., Filippenko, A. V., Challis, P., et al. 1998, *The Astronomical Journal*, 116, 1009, doi: [10.1086/300499](https://doi.org/10.1086/300499)
- Rodney, S. A., Brammer, G. B., Pierel, J. D. R., et al. 2021, *Nature Astronomy*, doi: [10.1038/s41550-021-01450-9](https://doi.org/10.1038/s41550-021-01450-9)
- Sako, M., Bassett, B., Connolly, B., et al. 2011, *The Astrophysical Journal*, 738, 162, doi: [10.1088/0004-637X/738/2/162](https://doi.org/10.1088/0004-637X/738/2/162)
- Schlegel, D. J., Finkbeiner, D. P., & Davis, M. 1998, *The Astrophysical Journal*, 500, 525, doi: [10.1086/305772](https://doi.org/10.1086/305772)
- Scolnic, D., & Kessler, R. 2016, *The Astrophysical Journal*, 822, L35, doi: [10.3847/2041-8205/822/2/L35](https://doi.org/10.3847/2041-8205/822/2/L35)
- Shu, Y., Bolton, A. S., Mao, S., et al. 2018, *The Astrophysical Journal*, 864, 91, doi: [10.3847/1538-4357/aad5ea](https://doi.org/10.3847/1538-4357/aad5ea)
- Shu, Y., Bolton, A. S., Mao, S., et al. 2021, *ApJ*, 919, 67, doi: [10.3847/1538-4357/ac24a4](https://doi.org/10.3847/1538-4357/ac24a4)
- Shu, Y., Brownstein, J. R., Bolton, A. S., et al. 2017, *ApJ*, 851, 48, doi: [10.3847/1538-4357/aa9794](https://doi.org/10.3847/1538-4357/aa9794)
- Shu, Y., Brownstein, J. R., Bolton, A. S., et al. 2017, *The Astrophysical Journal*, 851, 48, doi: [10.3847/1538-4357/aa9794](https://doi.org/10.3847/1538-4357/aa9794)
- Strolger, L.-G., Rodney, S. A., Pacifici, C., Narayan, G., & Graur, O. 2020, *The Astrophysical Journal*, 890, 140, doi: [10.3847/1538-4357/ab6a97](https://doi.org/10.3847/1538-4357/ab6a97)
- Strolger, L.-G., Dahlen, T., Rodney, S. A., et al. 2015, *The Astrophysical Journal*, 813, 93, doi: [10.1088/0004-637X/813/2/93](https://doi.org/10.1088/0004-637X/813/2/93)
- Sullivan, M., Borgne, D. L., Pritchett, C. J., et al. 2006, *The Astrophysical Journal*, 648, 868, doi: [10.1086/506137](https://doi.org/10.1086/506137)
- Suyu, S. H., Chang, T.-C., Courbin, F., & Okumura, T. 2018, *SSRv*, 214, 91, doi: [10.1007/s11214-018-0524-3](https://doi.org/10.1007/s11214-018-0524-3)
- Suyu, S. H., Bonvin, V., Courbin, F., et al. 2017, *MNRAS*, 468, 2590, doi: [10.1093/mnras/stx483](https://doi.org/10.1093/mnras/stx483)
- Treu, T., Dutton, A. A., Auger, M. W., et al. 2011, *MNRAS*, 417, 1601, doi: [10.1111/j.1365-2966.2011.19378.x](https://doi.org/10.1111/j.1365-2966.2011.19378.x)
- Wojtak, R., Hjorth, J., & Gall, C. 2019, *Monthly Notices of the Royal Astronomical Society*, 487, 3342, doi: [10.1093/mnras/stz1516](https://doi.org/10.1093/mnras/stz1516)
- Wong, K. C., Suyu, S. H., Chen, G. C. F., et al. 2020, *MNRAS*, 498, 1420, doi: [10.1093/mnras/stz3094](https://doi.org/10.1093/mnras/stz3094)
- Zhang, B. R., Childress, M. J., Davis, T. M., et al. 2017, *MNRAS*, 471, 2254, doi: [10.1093/mnras/stx1600](https://doi.org/10.1093/mnras/stx1600)

APPENDIX

A. DETAILS FOR OUR TARGET SYSTEMS

Table A1. The 98 target systems, with spectroscopic redshifts for lensing and source galaxies, magnifications, star formation rates [msol/yr], and (observer-frame) supernova rates [year⁻¹], with uncertainties. All taken from (Shu et al. 2018), with the correction factor of $(1 + z_s)^{-2}$ applied to his star formation rates.

Survey Name	z_L	z_S	μ	SFR	e_{SFR}	N_{cc}	e_{Ncc}	N_{Ia}	e_{NIa}
SDSSJ0029-0055	0.23	0.93	23	1.42	0.81	5.1e-03	2.9e-03	6.4e-04	3.6e-04
SDSSJ0037-0942	0.20	0.63	6	2.37	1.20	1.0e-02	5.2e-03	1.5e-03	7.5e-04
SDSSJ0044+0113	0.12	0.20	2	1.74	0.83	1.0e-02	4.8e-03	1.9e-03	9.1e-04
SDSSJ0109+1500	0.29	0.52	2	2.64	1.64	1.2e-02	7.6e-03	1.9e-03	1.2e-03
SDSSJ0157-0056	0.51	0.92	2	22.76	16.33	8.3e-02	5.9e-02	1.0e-02	7.4e-03
SDSSJ0216-0813	0.33	0.52	3	8.48	4.37	3.9e-02	2.0e-02	6.0e-03	3.1e-03
SDSSJ0252+0039	0.28	0.98	16	4.90	2.24	1.7e-02	7.9e-03	2.1e-03	9.6e-04
SDSSJ0330-0020	0.35	1.07	4	22.94	11.16	7.7e-02	3.8e-02	9.0e-03	4.4e-03
SDSSJ0405-0455	0.08	0.81	16	0.64	0.31	2.5e-03	1.2e-03	3.3e-04	1.6e-04
SDSSJ0728+3835	0.21	0.69	10	0.98	0.67	4.0e-03	2.7e-03	5.7e-04	3.9e-04
SDSSJ0737+3216	0.32	0.58	14	1.84	0.92	8.1e-03	4.1e-03	1.2e-03	6.1e-04
SDSSJ0822+2652	0.24	0.59	7	1.27	0.63	5.6e-03	2.8e-03	8.2e-04	4.1e-04
SWELLSJ0841+3824	0.12	0.66	5	-99.0	-99.0	-99.0	-99.0	-99.0	-99.0
SDSSJ0903+4116	0.43	1.06	8	6.34	4.88	2.1e-02	1.7e-02	2.5e-03	1.9e-03
SDSSJ0912+0029	0.16	0.32	6	1.43	0.92	7.6e-03	4.9e-03	1.3e-03	8.4e-04
SDSSJ0935-0003	0.35	0.47	3	3.19	3.05	1.5e-02	1.4e-02	2.4e-03	2.3e-03
SDSSJ0936+0913	0.19	0.59	7	1.19	0.63	5.2e-03	2.8e-03	7.7e-04	4.1e-04
SDSSJ0946+1006	0.22	0.61	18	1.77	0.93	7.7e-03	4.0e-03	1.1e-03	5.9e-04
SDSSJ0955+0101	0.11	0.32	4	1.21	0.57	6.4e-03	3.0e-03	1.1e-03	5.3e-04
SDSSJ0956+5100	0.24	0.47	8	1.34	0.74	6.4e-03	3.5e-03	1.0e-03	5.6e-04
SDSSJ0959+0410	0.13	0.54	5	2.07	1.31	9.4e-03	5.9e-03	1.4e-03	9.0e-04
SDSSJ0959+4416	0.24	0.53	9	0.81	0.43	3.7e-03	1.9e-03	5.7e-04	3.0e-04
SDSSJ1016+3859	0.17	0.44	5	0.77	0.48	3.7e-03	2.3e-03	6.0e-04	3.8e-04
SDSSJ1020+1122	0.28	0.55	6	1.37	0.79	6.2e-03	3.6e-03	9.4e-04	5.4e-04
SWELLSJ1029+0420	0.10	0.62	4	2.90	1.64	1.2e-02	7.1e-03	1.8e-03	1.0e-03
SDSSJ1032+5322	0.13	0.33	3	3.39	1.58	1.8e-02	8.3e-03	3.1e-03	1.4e-03
SDSSJ1100+5329	0.32	0.86	13	8.87	4.77	3.3e-02	1.8e-02	4.3e-03	2.3e-03
SDSSJ1103+5322	0.16	0.74	3	25.20	18.33	1.0e-01	7.4e-02	1.4e-02	1.0e-02
SDSSJ1106+5228	0.10	0.41	25	1.16	0.70	5.7e-03	3.5e-03	9.4e-04	5.7e-04
SDSSJ1112+0826	0.27	0.63	4	12.04	6.62	5.2e-02	2.8e-02	7.5e-03	4.1e-03
SDSSJ1142+1001	0.22	0.50	3	2.27	1.20	1.1e-02	5.6e-03	1.6e-03	8.7e-04
SDSSJ1143-0144	0.11	0.40	4	8.47	3.93	4.2e-02	2.0e-02	7.0e-03	3.2e-03
SDSSJ1153+4612	0.18	0.88	10	2.21	1.13	8.2e-03	4.2e-03	1.0e-03	5.3e-04
SDSSJ1204+0358	0.16	0.63	9	2.60	1.39	1.1e-02	6.0e-03	1.6e-03	8.6e-04
SDSSJ1205+4910	0.21	0.48	13	1.23	0.55	5.8e-03	2.6e-03	9.1e-04	4.1e-04
SDSSJ1213+6708	0.12	0.64	8	2.75	1.45	1.2e-02	6.2e-03	1.7e-03	8.9e-04
SDSSJ1250+0523	0.23	0.80	10	5.43	2.87	2.1e-02	1.1e-02	2.8e-03	1.5e-03
SDSSJ1251-0208	0.22	0.78	4	6.44	3.47	2.5e-02	1.4e-02	3.4e-03	1.8e-03
SDSSJ1416+5136	0.30	0.81	4	16.48	10.59	6.4e-02	4.1e-02	8.4e-03	5.4e-03

SDSSJ1420+6019	0.06	0.54	13	1.64	0.84	7.5e-03	3.8e-03	1.1e-03	5.8e-04
SDSSJ1430+4105	0.28	0.58	6	7.41	3.69	3.3e-02	1.6e-02	4.9e-03	2.4e-03
SDSSJ1432+6317	0.12	0.66	4	16.44	7.80	6.9e-02	3.3e-02	9.9e-03	4.7e-03
SDSSJ1436-0000	0.29	0.80	4	5.83	3.09	2.3e-02	1.2e-02	3.0e-03	1.6e-03
SDSSJ1443+0304	0.13	0.42	7	0.45	0.25	2.2e-03	1.2e-03	3.6e-04	2.0e-04
SDSSJ1451-0239	0.13	0.52	11	1.43	0.74	6.6e-03	3.4e-03	1.0e-03	5.2e-04
SDSSJ1525+3327	0.36	0.72	4	7.98	3.85	3.2e-02	1.6e-02	4.5e-03	2.2e-03
SDSSJ1538+5817	0.14	0.53	8	7.05	3.20	3.2e-02	1.5e-02	4.9e-03	2.2e-03
SDSSJ1621+3931	0.24	0.60	8	5.27	4.92	2.3e-02	2.1e-02	3.4e-03	3.2e-03
SDSSJ1627-0053	0.21	0.52	20	0.56	0.26	2.6e-03	1.2e-03	4.0e-04	1.8e-04
SDSSJ1630+4520	0.25	0.79	9	5.21	3.00	2.0e-02	1.2e-02	2.7e-03	1.6e-03
SDSSJ1636+4707	0.23	0.67	8	0.82	0.47	3.4e-03	1.9e-03	4.9e-04	2.8e-04
SDSSJ2238-0754	0.14	0.71	12	2.53	1.30	1.0e-02	5.3e-03	1.4e-03	7.4e-04
SDSSJ2300+0022	0.23	0.46	12	0.33	0.23	1.6e-03	1.1e-03	2.5e-04	1.8e-04
SDSSJ2303+1422	0.16	0.52	8	0.69	0.48	3.2e-03	2.2e-03	4.9e-04	3.4e-04
SDSSJ2321-0939	0.08	0.53	12	2.86	1.41	1.3e-02	6.4e-03	2.0e-03	9.8e-04
SDSSJ0143-1006	0.22	1.10	3	36.17	22.47	1.2e-01	7.5e-02	1.4e-02	8.6e-03
SDSSJ0159-0006	0.16	0.75	6	1.70	0.95	6.8e-03	3.8e-03	9.2e-04	5.1e-04
SDSSJ0324+0045	0.32	0.92	14	0.79	0.49	2.9e-03	1.8e-03	3.6e-04	2.2e-04
SDSSJ0324-0110	0.45	0.62	4	1.33	0.65	5.7e-03	2.8e-03	8.4e-04	4.1e-04
SDSSJ0753+3416	0.14	0.96	27	2.92	1.64	1.0e-02	5.8e-03	1.3e-03	7.2e-04
SDSSJ0754+1927	0.15	0.74	5	5.91	3.60	2.4e-02	1.4e-02	3.2e-03	2.0e-03
SDSSJ0757+1956	0.12	0.83	9	8.48	4.48	3.2e-02	1.7e-02	4.2e-03	2.2e-03
SDSSJ0847+2348	0.16	0.53	17	0.34	0.17	1.6e-03	7.8e-04	2.4e-04	1.2e-04
SDSSJ0851+0505	0.13	0.64	6	3.09	1.67	1.3e-02	7.1e-03	1.9e-03	1.0e-03
SDSSJ0920+3028	0.29	0.39	8	0.57	0.26	2.9e-03	1.3e-03	4.7e-04	2.2e-04
SDSSJ0955+3014	0.32	0.47	4	0.83	0.83	4.0e-03	4.0e-03	6.3e-04	6.3e-04
SDSSJ1010+3124	0.17	0.42	4	2.43	1.24	1.2e-02	6.1e-03	1.9e-03	9.9e-04
SDSSJ1031+3026	0.17	0.75	5	6.53	3.40	2.6e-02	1.4e-02	3.5e-03	1.8e-03
SDSSJ1040+3626	0.12	0.28	3	0.49	0.24	2.7e-03	1.3e-03	4.7e-04	2.4e-04
SDSSJ1041+0112	0.10	0.22	5	0.20	0.13	1.2e-03	7.7e-04	2.1e-04	1.4e-04
SDSSJ1048+1313	0.13	0.67	4	6.56	6.53	2.7e-02	2.7e-02	3.9e-03	3.9e-03
SDSSJ1051+4439	0.16	0.54	3	7.29	3.71	3.3e-02	1.7e-02	5.0e-03	2.6e-03
SDSSJ1056+4141	0.13	0.83	10	1.85	0.87	7.1e-03	3.3e-03	9.2e-04	4.3e-04
SDSSJ1101+1523	0.18	0.52	5	1.51	0.82	7.0e-03	3.8e-03	1.1e-03	5.8e-04
SDSSJ1127+2312	0.13	0.36	8	2.27	1.08	1.2e-02	5.5e-03	2.0e-03	9.4e-04
SDSSJ1137+1818	0.12	0.46	10	1.74	0.84	8.3e-03	4.0e-03	1.3e-03	6.4e-04
SDSSJ1142+2509	0.16	0.66	18	0.58	0.29	2.4e-03	1.2e-03	3.5e-04	1.7e-04
SDSSJ1144+0436	0.10	0.26	5	0.94	0.50	5.2e-03	2.8e-03	9.4e-04	5.0e-04
SDSSJ1213+2930	0.09	0.60	21	0.78	0.43	3.4e-03	1.9e-03	5.0e-04	2.8e-04
SDSSJ1301+0834	0.09	0.53	9	2.48	2.14	1.1e-02	9.7e-03	1.7e-03	1.5e-03
SDSSJ1330+1750	0.21	0.37	4	1.01	0.48	5.2e-03	2.4e-03	8.7e-04	4.1e-04
SDSSJ1433+2835	0.09	0.41	10	1.11	0.55	5.5e-03	2.7e-03	9.0e-04	4.5e-04
SDSSJ1541+3642	0.14	0.74	16	2.28	1.06	9.1e-03	4.2e-03	1.2e-03	5.8e-04
SDSSJ1543+2202	0.27	0.40	3	3.42	1.58	1.7e-02	7.9e-03	2.8e-03	1.3e-03
SDSSJ1550+2020	0.14	0.35	2	3.95	1.98	2.0e-02	1.0e-02	3.5e-03	1.7e-03
SDSSJ1553+3004	0.16	0.57	5	2.23	1.10	9.9e-03	4.9e-03	1.5e-03	7.3e-04
SDSSJ1607+2147	0.21	0.49	2	2.07	1.17	9.7e-03	5.5e-03	1.5e-03	8.6e-04
SDSSJ1633+1441	0.13	0.58	19	1.04	0.52	4.6e-03	2.3e-03	6.8e-04	3.4e-04
SDSSJ2309-0039	0.29	1.00	4	11.53	8.07	4.0e-02	2.8e-02	4.8e-03	3.4e-03

BELLSJ0830+5116	0.53	1.33	6	24.68	15.93	7.4e-02	4.8e-02	7.6e-03	4.9e-03
BELLSJ1159-0007	0.58	1.35	8	14.74	7.03	4.4e-02	2.1e-02	4.5e-03	2.1e-03
BELLSJ1221+3806	0.53	1.28	4	18.70	10.85	5.7e-02	3.3e-02	6.0e-03	3.5e-03
BELLSJ1318-0104	0.66	1.40	7	11.86	6.30	3.4e-02	1.8e-02	3.5e-03	1.8e-03
BELLSJ1337+3620	0.56	1.18	12	9.76	6.12	3.1e-02	2.0e-02	3.5e-03	2.2e-03
BELLSJ1349+3612	0.44	0.89	5	6.61	3.14	2.4e-02	1.2e-02	3.1e-03	1.5e-03
BELLSJ1542+1629	0.35	1.02	3	14.02	11.27	4.8e-02	3.9e-02	5.8e-03	4.6e-03
BELLSJ1601+2138	0.54	1.45	3	25.22	19.89	7.2e-02	5.7e-02	7.1e-03	5.6e-03
BELLSJ1631+1854	0.41	1.09	19	13.62	6.39	4.5e-02	2.1e-02	5.2e-03	2.5e-03

Table A2. The 98 target systems, with data for our observations of each source. This includes the number of observations across the survey.

Survey Name	Number of observations	Average Seeing (Arcseconds)	Average Airmass
BELLSJ0830+5116	10	8.56	1.34
BELLSJ1159-0007	19	4.7	1.33
BELLSJ1221+3806	14	12.39	1.36
BELLSJ1318-0104	22	5.93	1.38
BELLSJ1337+3620	15	7.63	1.32
BELLSJ1349+3612	12	7.38	1.27
BELLSJ1542+1629	22	5.94	1.49
BELLSJ1601+2138	11	12.34	1.2
BELLSJ1631+1854	22	6.71	1.51
SDSSJ0029-0055	23	6.19	1.39
SDSSJ0037-0942	20	5.27	1.27
SDSSJ0044+0113	25	5.81	1.4
SDSSJ0109+1500	23	3.92	1.46
SDSSJ0143-1006	19	4.78	1.35
SDSSJ0157-0056	22	4.82	1.37
SDSSJ0159-0006	23	4.86	1.36
SDSSJ0216-0813	23	5.34	1.34
SDSSJ0252+0039	19	5.55	1.34
SDSSJ0324+0045	21	4.21	1.43
SDSSJ0324-0110	26	8.26	1.31
SDSSJ0330-0020	20	6.96	1.37
SDSSJ0405-0455	30	5.33	1.31
SDSSJ0728+3835	18	10.42	1.36
SDSSJ0737+3216	13	11.33	1.36
SDSSJ0753+3416	13	9.72	1.3
SDSSJ0754+1927	16	4.24	1.54
SDSSJ0757+1956	18	7.7	1.55
SDSSJ0822+1828	3	3.34	1.58
SDSSJ0822+2652	18	8.39	1.57
SDSSJ0847+2348	19	7.56	1.52
SDSSJ0851+0505	23	4.1	1.36
SDSSJ0903+4116	13	9.07	1.26
SDSSJ0912+0029	21	9.0	1.33
SDSSJ0920+3028	18	11.65	1.31
SDSSJ0935-0003	22	7.21	1.38

SDSSJ0936+0913	21	6.58	1.44
SDSSJ0946+1006	18	6.0	1.47
SDSSJ0955+0101	21	5.09	1.31
SDSSJ0955+3014	16	9.81	1.34
SDSSJ0956+5100	12	11.4	1.42
SDSSJ0959+0410	22	5.44	1.4
SDSSJ0959+4416	15	10.52	1.31
SDSSJ1010+3124	15	10.13	1.37
SDSSJ1016+3859	13	18.33	1.33
SDSSJ1020+1122	19	8.21	1.48
SDSSJ1031+3026	11	14.82	1.32
SDSSJ1032+5322	16	7.82	1.32
SDSSJ1040+3626	15	13.11	1.35
SDSSJ1041+0112	22	6.75	1.37
SDSSJ1048+1313	23	4.9	1.51
SDSSJ1051+4439	14	7.81	1.34
SDSSJ1056+4141	15	11.49	1.26
SDSSJ1100+5329	12	5.25	1.38
SDSSJ1101+1523	20	5.85	1.52
SDSSJ1103+5322	14	8.08	1.39
SDSSJ1106+5228	14	7.22	1.47
SDSSJ1112+0826	23	7.54	1.45
SDSSJ1127+2312	16	10.96	1.55
SDSSJ1137+1818	20	8.74	1.5
SDSSJ1142+1001	23	5.92	1.47
SDSSJ1142+2509	15	9.72	1.42
SDSSJ1143-0144	21	6.54	1.36
SDSSJ1144+0436	21	8.76	1.43
SDSSJ1153+4612	13	9.87	1.32
SDSSJ1204+0358	25	4.99	1.42
SDSSJ1205+4910	17	12.66	1.39
SDSSJ1213+2930	14	9.97	1.27
SDSSJ1213+6708	17	10.95	1.47
SDSSJ1250+0523	22	3.33	1.39
SDSSJ1251-0208	24	6.48	1.44
SDSSJ1301+0834	27	5.85	1.42
SDSSJ1330+1750	25	4.77	1.51
SDSSJ1416+5136	16	11.82	1.41
SDSSJ1420+6019	17	8.51	1.39
SDSSJ1430+4105	16	6.35	1.34
SDSSJ1432+6317	14	11.36	1.39
SDSSJ1433+2835	11	11.03	1.34
SDSSJ1436-0000	28	5.66	1.41
SDSSJ1443+0304	24	6.49	1.42
SDSSJ1451-0239	24	4.88	1.4
SDSSJ1525+3327	19	13.83	1.35
SDSSJ1538+5817	14	6.78	1.43
SDSSJ1541+3642	16	10.71	1.35
SDSSJ1543+2202	14	8.17	1.3
SDSSJ1550+2020	16	5.61	1.45

SDSSJ1553+3004	13	7.67	1.29
SDSSJ1607+2147	14	12.72	1.26
SDSSJ1621+3931	15	9.59	1.26
SDSSJ1627-0053	27	5.09	1.4
SDSSJ1630+4520	14	12.36	1.33
SDSSJ1633+1441	21	4.26	1.49
SDSSJ1636+4707	19	10.83	1.32
SDSSJ2238-0754	21	8.01	1.33
SDSSJ2300+0022	22	4.64	1.39
SDSSJ2303+1422	21	7.34	1.44
SDSSJ2309-0039	19	6.38	1.37
SDSSJ2321-0939	23	7.01	1.33
SWELLSJ0820+4847	11	13.08	1.39
SWELLSJ0822+1828	16	6.39	1.53
SWELLSJ0841+3824	15	15.29	1.25
SWELLSJ0915+4211	12	8.25	1.32
SWELLSJ0930+2855	13	9.45	1.28
SWELLSJ0955+0101	2	2.9	1.44
SWELLSJ1021+2028	17	7.25	1.55
SWELLSJ1029+0420	22	5.77	1.4
SWELLSJ1037+3517	11	5.65	1.3
SWELLSJ1111+2234	13	8.28	1.43
SWELLSJ1117+4704	13	8.74	1.3
SWELLSJ1135+3720	16	9.7	1.34
SWELLSJ1203+2535	16	16.7	1.27
SWELLSJ1313+0506	22	5.38	1.42
SWELLSJ1331+3638	14	11.96	1.39
SWELLSJ1703+2451	15	10.94	1.29
SWELLSJ2141-0001	22	9.08	1.35